Keldysh Institute • Publication search

Keldysh Institute preprints • Preprint No. 82, 2018

ISSN 2071-2898 (Print)
ISSN 2071-2901 (Online)

Zaitsev N.A., **Sofronov I.L.**

Generation of transparent boundary conditions for modeling wave propagation in anisotropic media

Recommended form of bibliographic references: Zaitsev N.A., Sofronov I.L. Generation of transparent boundary conditions for modeling wave propagation in anisotropic media // Keldysh Institute Preprints. 2018. No. 82. 36 p. doi:10.20948/prepr-2018-82-e
URL: http://library.keldysh.ru/preprint.asp?id=2018-82&lg=e

О р д е н а Л е н и н а
ИНСТИТУТ ПРИКЛАДНОЙ МАТЕМАТИКИ
имени М.В.Келдыша
Р о с с и й с к о й а к а д е м и и н а у к

N. A. Zaitsev, I. L. Sofronov

Generation of transparent boundary conditions for modeling wave propagation in anisotropic media

Москва — 2018

Зайцев Н. А., Софронов И. Л.

Построение прозрачных граничных условий для моделирования распространения волн в анизотропных средах

Препринт содержит математические основы и численные методы для построения условий полной прозрачности (УПП) для ортотропных сред. Рассмотрена двумерная задача распространения волн в полярных координатах.

Ключевые слова: неотражающие граничные условия, условия полной прозрачности, анизотропные среды, динамические задачи упругости

N. A. Zaitsev, I. L. Sofronov

Generation of transparent boundary conditions for modeling wave propagation in anisotropic media

The preprint contains results on development of mathematical foundations and numerical approaches of generating transparent boundary conditions (TBCs) for orthotropic anisotropic elastic media. A two-dimensional wave propagation problem in polar coordinates (r, θ) is considered.

Key words: non-reflecting boundary conditions, transparent boundary conditions, anisotropic media, dynamic elastic problems

Оглавление

Introduction

Numerical modeling of wave propagation in rock with anisotropic properties is the challenging problem. One of main difficulties of the physical phenomena consists of necessity to resolve accurately much more complicated wave fronts picture comparing to the case of isotropic media.

The original problem of the wave propagation is usually considered in unbounded media. However, numerical methods can only use bounded computational domains. Evidently, so-called “open boundaries” of computational domains must be genuine transparent for outgoing waves: otherwise, the spurious reflections strongly change the solution. That is why the generation of reliable low-reflecting boundary conditions on the open boundaries in anisotropic media is a crucial task for numerical modeling.

A typical setup is shown in Figure 1. The original problem is formulated in the whole space or in some unbounded domain whereas we want to know the solution in a bounded domain Ω_0 — observation domain or domain of interest. It is desirable to have the computational domain Ω as small as possible (of course, $\Omega_o \subseteq \Omega$). The original problem formulation may have some boundaries, internal or external, for which there are natural correct conditions based on properties of physical phenomena. In order to make the computational domain bounded we have to add some artificial boundary $\mathbf{\Gamma}$ which originally is free of boundary conditions — it belongs to interior of the problem formulation domain where only the governing equations should be satisfied. The open boundary here is the circle $\mathbf{\Gamma}$, the computational domain Ω is the interior of $\mathbf{\Gamma}$.

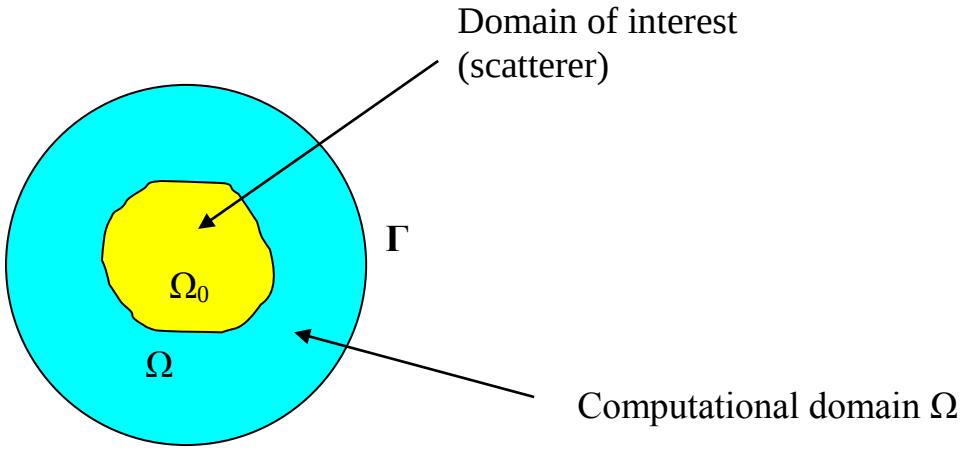

Figure 1. A computational domain and open boundary Γ

We have to state at **Γ** the corresponding boundary conditions which at least provide correctness of the corresponding Initial-Boundary Value Problem (IBVP). Among all possible boundary conditions providing the uniqueness there exists a set of boundary conditions that give solutions which are more or less close to the solution of the original problem. But we want to construct the exact boundary conditions. The boundary conditions are said to be exact, if solutions of the problem computed in the restricted domain Ω with these conditions are identical to restrictions to Ω of the corresponding solutions of the original problem in the whole space with the same governing data (initial and/or boundary values).

Applying to acoustic problems such coincidence of the solutions means that these boundary conditions permit outgoing waves, or disturbances, to leave Ω without any "reflection" from artificial boundary **Γ**. That is why we call such boundary condition operator a Transparent Boundary Conditions (TBC) operator. We can also call these conditions *equivalent* boundary conditions because satisfying TBC on Γ is equivalent to solving the problem in the whole space outside Ω.

Evidently, generation of TBC is a separate task (even for a given geometry and media inside **Γ**) which is formulated by considering auxiliary external initial-boundary-valued problems outside **Γ**.

Let the medium outside **Γ** and in some vicinity of **Γ** inside it is a linear anisotropic elastic medium with constant coefficients. Let the right hand side of the governing equations is equal to zero outside **Γ**. And let disturbances outside **Γ** are absent at the initial time moment. Then we can compute the TBC on **Γ**.

Remark. In the domain of interest the governing equations and geometry can be much more complex than outside it.

It is known that the popular PML approach can fail in elastodynamics with anisotropy (though it is good enough for many isotropic cases). The PML method does not work here when both "outgoing" and "incoming" wave fronts present on the open border of the computational domain; such case is out of the framework of the base idea of the method, see de-tails in [1]-[2]. However, the original wave problem formulated on the unbounded domain is the well-posed one, i.e. there are no physical restrictions to have desired TBC.

We have developed TBCs for such problems and numerical methods for their implementations and for calculation of coefficients of the TBC operator. The approach was announced in [3], some results of their application were given in [4]. Also in [4] was announced a detailed description of the correspondent numerical method to compute operators of the TBCs. Here we present the announced numerical method and some numerical tests that demonstrate the accuracy and stability of the problems with our TBCs.

§ 1. Governing equations

The equations of motion in an elastic medium in Cartesian coordinates are

$$\rho \frac{\partial^2 u^i}{\partial t^2} = \frac{\partial \sigma^{ij}}{\partial x_j} + h^i$$

(we use the Einstein notation for implicit sums over repeating indexes in a term). Here ρ is the density, u^i are Cartesian components of displacements, h^i is an external force per unit volume, and the stress tensor σ^{ij} is related to the tensor of deformation

$$\varepsilon_{ij} = \frac{1}{2}\left(\frac{\partial u^i}{\partial x_j} + \frac{\partial u^j}{\partial x_i} \right)$$

by Hooke's law

$$\sigma^{ij} = c^{ij,kl} \varepsilon_{kl}. \tag{1}$$

Here $c^{ij,kl}$ is the tensor of elastic coefficients (which is constant in case of homogenous media).

Tensors σ, c and ε are symmetric. In their indices, we replace pairs "11" by "1", "22" by "2", and "12" and "21" by "3" (with $\varepsilon_3 = \varepsilon_{12} + \varepsilon_{21} = 2\varepsilon_{12} = 2\varepsilon_{21}$). Hooke's law (1) then becomes

$$\sigma^n = c^{nm} \varepsilon_m, \quad n \in \{1,2,3\}. \tag{2}$$

Due to symmetry, $c^{nm} = c^{mn}$. For orthotropic media with principal axes coinciding with x_1 and x_2, we have $c^{13} = c^{23} = 0$.

In the 2D case in polar coordinates the equations of motion are

$$\begin{aligned} \rho \frac{\partial^2 u^r}{\partial t^2} &= \frac{\partial \sigma^{rr}}{\partial r} + \frac{1}{r}\frac{\partial \sigma^{r\theta}}{\partial \theta} + \frac{\sigma^{rr} - \sigma^{\theta\theta}}{r} + h^r, \\ \rho \frac{\partial^2 u^\theta}{\partial t^2} &= \frac{\partial \sigma^{r\theta}}{\partial r} + \frac{1}{r}\frac{\partial \sigma^{\theta\theta}}{\partial \theta} + \frac{2\sigma^{r\theta}}{r} + h^\theta. \end{aligned} \tag{3}$$

Here u^r and u^θ are the displacements expressed in local physical coordinates. The tensor of deformations in polar coordinates is

$$\varepsilon_{rr} = \frac{\partial u^r}{\partial r}, \quad \varepsilon_{\theta\theta} = \frac{1}{r}\frac{\partial u^\theta}{\partial \theta} + \frac{u_r}{r}, \quad 2\varepsilon_{r\theta} = \frac{1}{r}\frac{\partial u^r}{\partial \theta} + \frac{\partial u^\theta}{\partial r} - \frac{u^\theta}{r}. \tag{4}$$

Hooke's law is

$$\sigma^{ij} = c_P^{ij,kl}\varepsilon_{kl}, \tag{5}$$

where $c_P^{ij,kl}$ are physical components of the elasticity tensor, which have the following relations with Cartesian components:

$$c_P^{ij,kl} = b_I^i b_J^j b_K^k b_L^l c^{IJ,KL},$$

where

$$b_j^i = \begin{pmatrix} \cos\theta & \sin\theta \\ -\sin\theta & \cos\theta \end{pmatrix}.$$

Formula (5) becomes, after replacing in indices "rr" by 1, "$\theta\theta$" by 2, and "$r\theta$" by 3 (with $\varepsilon_3 = \varepsilon_{r\theta} + \varepsilon_{\theta r} = 2\varepsilon_{r\theta} = 2\varepsilon_{\theta r}$),

$$\sigma^n = c_P^{nm}\varepsilon_m, \quad n \in \{1,2,3\}. \tag{6}$$

Besides symmetry relation $c_P^{mn} = c_P^{nm}$, we also have $c_P^{11} = c_P^{22}$ and $c_P^{13} = c_P^{23}$ for cylindrical anisotropy.

After excluding components of the stress tensor σ using (6) and (4) equations (3) in the absence of external forces read:

$$\frac{\partial^2 f}{\partial t^2} = A^{11}\frac{\partial^2 f}{\partial r^2} + A^{22}\frac{\partial^2 f}{\partial \theta^2} + A^{12}\frac{\partial^2 f}{\partial r \partial \theta} + A^1\frac{\partial f}{\partial r} + A^2\frac{\partial f}{\partial \theta} + A^0 f \tag{7}$$

where $f = (u^r, u^\theta)^T$,

$$A^{11} = \rho^{-1}\begin{pmatrix} c_P^{11} & c_P^{13} \\ c_P^{13} & c_P^{33} \end{pmatrix}, \quad A^{22} = \rho^{-1}r^{-2}\begin{pmatrix} c_P^{33} & c_P^{23} \\ c_P^{23} & c_P^{22} \end{pmatrix},$$

$$A^{12} = \rho^{-1}r^{-1}\begin{pmatrix} 2c_P^{13} & c_P^{33} + c_P^{12} \\ c_P^{33} + c_P^{12} & 2c_P^{23} \end{pmatrix},$$

$$A^1 = \rho^{-1}r^{-1}\begin{pmatrix} c_P^{11} + \dfrac{\partial c_P^{13}}{\partial \theta} & -c_P^{23} + \dfrac{\partial c_P^{33}}{\partial \theta} \\ 2c_P^{13} + c_P^{23} + \dfrac{\partial c_P^{12}}{\partial \theta} & c_P^{33} + \dfrac{\partial c_P^{23}}{\partial \theta} \end{pmatrix},$$

$$A^2 = \rho^{-1} r^{-2} \begin{pmatrix} \dfrac{\partial}{\partial\theta} c_P^{33} & -c_P^{22} - c_P^{33} + \dfrac{\partial c_P^{23}}{\partial\theta} \\ c_P^{33} + c_P^{22} + \dfrac{\partial c_P^{23}}{\partial\theta} & \dfrac{\partial c_P^{22}}{\partial\theta} \end{pmatrix},$$

$$A^0 = \rho^{-1} r^{-2} \begin{pmatrix} -c_P^{22} + \dfrac{\partial c_P^{23}}{\partial\theta} & c_P^{23} - \dfrac{\partial c_P^{33}}{\partial\theta} \\ c_P^{23} + \dfrac{\partial c_P^{22}}{\partial\theta} & -c_P^{33} - \dfrac{\partial c_P^{23}}{\partial\theta} \end{pmatrix}.$$

Remark. Matrices in (7) do not depend on time, so components of velocities satisfy exactly the same equation. So we will consider components of velocities as unknown functions rather than components of displacements because it is more convenient for practical problems.

§ 2. Generation of TBC

Let us consider the homogeneous governing equations (7) outside Γ written formally in the operator form $f_{tt} - Lf = 0$ (see Figure 2). Function f can be represented on the circle $r = R_\Gamma$ as Fourier series:

$$f \equiv \begin{pmatrix} u_r \\ u_\theta \end{pmatrix} = \begin{pmatrix} U_{r,c}^0 + \sum_{m=1}^{\infty} \left(U_{r,c}^m \cos(m\theta) + U_{r,s}^m \sin(m\theta) \right) \\ U_{\theta,c}^0 + \sum_{m=1}^{\infty} \left(U_{\theta,c}^m \cos(m\theta) + U_{\theta,s}^m \sin(m\theta) \right) \end{pmatrix}.$$

One can see that each m-th Forier harmonic contains four independent basis functions that correspond to four Fourier coefficients: $U_{r,c}^m$, $U_{r,s}^m$, $U_{\theta,c}^m$ and $U_{\theta,s}^m$. It is convenient to numerate the basis function as a single sequence: $\{\varphi^m(\theta), m = 1,2,3,...\}$, so that $f(t,\theta) = \sum_m c_m(t)\varphi^m(\theta)$.

TBC operator is obtained after the following steps:

Stage 1: Consider set of auxiliary external initial boundary-value problems (IBVPs) outside the circle S with the boundary Γ (set wrt "m"):

$$\begin{cases} f_{tt} - Lf = 0 & \text{in} \quad \mathbb{R}^2 / S \\ f\big|_{t=0} = 0 \\ f\big|_\Gamma = \delta(t)\varphi^m(\theta) \end{cases} \tag{8}$$

where $\delta(t)$ is the Dirac delta function; $\{\varphi^m(\theta)\}_{m=0}^{\infty}$ is the basis on Γ consisting of set sinuses and cosines $\{\sin m\theta, \cos m\theta\}$, i.e. $f(t,\theta) = \sum_m c_m(t)\varphi^m(\theta)$.

Let $f^m(r,\theta,t)$ be the solution of the m-th problem (8).

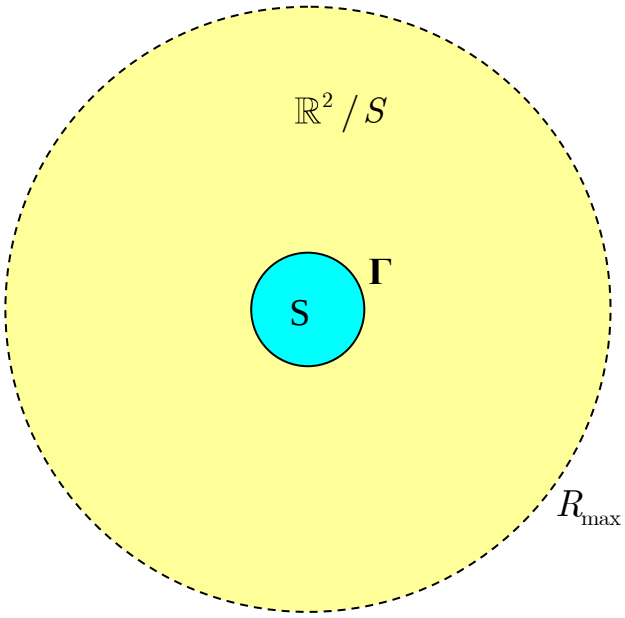

Figure 2. Outline of the auxiliary external problems

Stage 2: Make the Laplace transform and pass to set of elliptic BVPs (parameterized by s):

$$\begin{cases} s^2\hat{f} - L\hat{f} = 0 \quad \text{in} \quad \mathbb{R}^2 / S \\ \hat{f}\big|_{\Gamma} = \varphi^m(\theta) \\ \hat{f} \to 0 \qquad\quad \text{at} \quad \text{infinity} \end{cases} \tag{9}$$

Stage 3: Solve (numerically) the problems and evaluate $\frac{\partial}{\partial r}\hat{f}^m(r,\theta)$ on Γ. Thus, we obtain the Dirichlet-to-Neumann maps

$$\varphi^m(\theta) \mapsto \psi^m(\theta)[s] \qquad \left(\equiv \frac{\partial}{\partial r}\hat{f}^m(\theta, r),\ r = R_{\Gamma} \right).$$

Stage 4: Form matrix of the Poincare-Steklov operator by taking arbitrary data on Γ

$$\hat{f}(r,\theta,s)\big|_{\Gamma} = \sum_m \hat{c}_m(s)\varphi^m(\theta)$$

and writing out the representation of its normal derivative on Γ

$$\left.\frac{\partial \hat{f}^m(r,\theta,s)}{\partial r}\right|_{\Gamma} = \sum_m \hat{c}_m(s)\psi^m(\theta)[s] \equiv \sum_m \hat{c}_m(s)\sum_n P_n^m(s)\varphi^n(\theta),$$

where $P_n^m(s)$ are the Fourier coefficients of $\psi^m(\theta)$.

Thus, we obtain the Poincare-Steklov operator in space of Fourier coefficients:

$$\frac{\partial \hat{c}_n(s)}{\partial r} = \sum_n \hat{P}_n^m(s)\hat{c}_m(s)$$

or, in matrix form:

$$\frac{\partial \hat{\mathbf{c}}(s)}{\partial r} = \hat{\mathbf{P}}(s)\hat{\mathbf{c}}(s)$$

with $\hat{\mathbf{c}} = \left\{\hat{c}_0, \hat{c}_1, \ldots\right\}^T$. (Here we use symbolic notation for the Fourier coefficients of the normal derivative of $\hat{u}(s,\theta)$:

$$\frac{\partial}{\partial r}\hat{u}(s,\theta) = \sum_n \frac{\partial \hat{c}_n(s)}{\partial r}\varphi^n(\theta)\ .$$

Stage 5: Make inverse Laplace transform for the Poincare-Steklov operator. This procedure is made numerically. First, we represent matrix $\hat{\mathbf{P}}(s)$ by sum of three matrices in order to separate asymptotic at $s \to \infty$:

$$\hat{\mathbf{P}}(s) = \mathbf{P}_1 s + \mathbf{P}_0 + \hat{\mathbf{K}}(s); \quad \mathbf{P}_1, \mathbf{P}_0 \text{ are } consts, \quad \hat{\mathbf{K}}(s) = o(1). \tag{10}$$

Then we calculate rational approximations to each entry in $\hat{\mathbf{K}}(s)$ such that all poles have negative real parts, i.e.

$$\hat{K}_n^m(s) \approx \hat{\tilde{K}}_n^m(s) \equiv \sum_{l=1}^{L_n^m} \frac{\alpha_{n\,l}^m}{s - \beta_{n\,l}^m}, \quad \mathrm{Re}(\beta_{n\,l}^m) \le \delta < 0.$$

As it is known the rational representation admits analytical inversion of $\hat{\tilde{K}}_n^m(s)$.

Thus, the approximate analytical inverse Laplace transform of $\dfrac{\partial \hat{\mathbf{c}}(s)}{\partial r} = \hat{\mathbf{P}}(s)\hat{\mathbf{c}}(s)$ has the form:

$$\frac{\partial \mathbf{c}(t)}{\partial r} \approx \mathbf{P}_1 \frac{\partial \mathbf{c}(t)}{\partial t} + \mathbf{P}_0 \mathbf{c}(t) + \tilde{\mathbf{K}}(t) * \mathbf{c}(t)$$

with the explicit kernels $\tilde{K}_n^m(t)$:

$$\tilde{K}_n^m(t) = \sum_{l=1}^{L_n^m} \alpha_{n\,l}^m \exp(\beta_{n\,l}^m t), \qquad \mathrm{Re}(\beta_{n\,l}^m) \le \delta < 0 .$$

Stage 6: Formulate TBC operator in physical space. We introduce $\mathbf{Q}$, the operator of Fourier decomposition for

$$f(t,\theta) = \sum_m c_m(t)\varphi^m(\theta)$$

i.e.

$$\mathbf{Q} : f(t,\theta) \to \{c_m(t)\}.$$

Finally we obtain the following relationship between functions and derivatives on Γ:

$$\mathbf{Q}^{-1}\mathbf{P}_1\mathbf{Q}\frac{\partial f}{\partial t} - \frac{\partial f}{\partial r} + \mathbf{Q}^{-1}\mathbf{P}_0\mathbf{Q}f + \mathbf{Q}^{-1}\left\{\tilde{\mathbf{K}}(t)*\right\}\mathbf{Q}f = 0 \qquad (11)$$

This equation is our desired TBC.

Let us mention some numerical aspects.

Stages 1–6: we take discrete basis on the uniform azimuth grid

$$\theta_k = k\frac{2\pi}{N_\theta},\ k = 1,\ldots,N_\theta, \qquad (12)$$

for the radial and azimuth components:

$$f_r(\theta_k) = \sum_{m=1}^{N_M-1} f_{r,m}^{si}\sin(m\theta_k) + \sum_{m=0}^{N_M} f_{r,m}^{co}\cos(m\theta_k),$$

$$f_\theta(\theta_k) = \sum_{m=1}^{N_M-1} f_{\theta,m}^{si}\sin(m\theta_k) + \sum_{m=0}^{N_M} f_{\theta,m}^{co}\cos(m\theta_k),$$

where N_M is the highest Fourier harmonics treated by approximate TBCs, and write the transformation in the matrix form

$$\begin{Bmatrix} f_r(\theta_k)_{k=1..N_\theta} \\ \\ f_\theta(\theta_k)_{k=1..N_\theta} \end{Bmatrix} = \mathbf{Q}_M^{-1} \begin{Bmatrix} \begin{Bmatrix} f_{r,0}^{co} \\ f_{\theta,0}^{co} \end{Bmatrix} \\ \begin{Bmatrix} f_{r,m}^{co} \\ f_{\theta,m}^{si} \\ f_{r,m}^{si} \\ f_{\theta,m}^{co} \end{Bmatrix}_{m=1...N_M} \end{Bmatrix}. \qquad (13)$$

Here the left vector is column of two sets with N_θ values; the right vector is column of N_M quadruples except for the top pair $(m = 0)$.

Stage 2 [Laplace image]: we take a finite interval $[0, S_{\max}]$ and choose set of knots $\{s_j\} \in [0, S_{\max}]$ which are representative enough to use discrete counterparts $\hat{K}_n^m(s_j)$ of kernels for the rational approximation (Stage 5). Currently $\{s_j\}_{j=1}^J$ are nodes of the Chebyshev's grid

$$s_j = \frac{S_{\max}}{2}\left(1 - \cos\left(\pi(j-0.5)/J\right)\right), \quad j = 1,...,J\,.$$

The magnitude of $S_{\max}$ depends on the number of harmonics m like $S_{\max} = O(m)$.

Stages 3-4 [Poincare-Steklov operator]: For each given s_j we discretise problem (9). Thus we have J elliptic problems. Each problem is solved on the set of finer and finer grids unless the so-called mesh convergence to a given residual ε achieves. These grids with doubled number of nodes permit to use the Richardson extrapolation increasing essentially the accuracy of our solution.

The radius $R_{\max}$ of the outer boundary is unknown in advance. Therefore we make also calculations with greater and greater value of $R_{\max}$ unless the difference between solutions becomes less than ε.

Further details of the algorithm see below.

Stage 5 [inverse Laplace transform]. After running the previous stages we have set of matrices $\hat{\mathbf{P}}(s_j)$ depending of s_j. For each entry $\hat{P}_n^m(s_j)$ we make asymptotic decomposition

$$\hat{P}_n^m(s) = P_{1,n}^m s + P_{0,n}^m + o(1), \quad \text{as} \quad s \to \infty$$

Estimation of constants $P_{1,n}^m$, $P_{0,n}^m$ is made by analyzing the rational approximation

$$R_n^m(s_j) \approx \hat{P}_n^m(s_j)$$

on the interval $[0, S_{\max}]$ with help of the Chebyshev-Padé algorithm.

Afterwards, we form the matrix $\hat{\mathbf{K}}(s_j) := \hat{\mathbf{P}}(s_j) - \mathbf{P}_1 s_j - \mathbf{P}_0$ and find (numerically) the rational approximations of entries $\hat{K}_n^m(s_j)$ on the set $\{s_j\}_{j=1}^J$ by an optimization algorithm minimizing the residual

$$\left\| \hat{K}(s_j) - \sum_{l=1}^{L} \frac{\alpha_l}{s_j - \beta_l} \right\|^2_{\{s_j\}} \to \min_{\alpha_l, \beta_l}, \ \operatorname{Re}(\beta_l) \le \delta < 0;$$

here the indices $\binom{m}{n}$ at terms K, L, α, β are omitted for clarity.

As a result, we obtain the rational functions $\hat{\tilde{K}}_n^m(s)$ satisfying inequality

$$| \hat{K}_n^m(s_j) - \hat{\tilde{K}}_n^m(s_j) | < \varepsilon_R$$

on the interval $[0, S_{\max}]$. These functions are explicitly inverted from the Laplace space:

$$\hat{\tilde{K}}_n^m(s) \mapsto \tilde{K}_n^m(t) \equiv \sum_{l=1}^{L_n^m} \alpha_{n\,l}^m \exp(\beta_{n\,l}^m t), \qquad \operatorname{Re}(\beta_{n\,l}^m) \le \delta < 0$$

Thus for each entry $\hat{P}_n^m(s_j)$ we find set of approximating parameters

$$P_{1,n}^m, \ P_{0,n}^m, \ L_n^m, \ \left\{ \alpha_{n\,l}^m, \beta_{n\,l}^m \right\}_{l=1}^{L_n^m}$$

Further details of the algorithm see below.

Stage 6 [approximate TBC]: We introduce a parameter $N_{M_H} \geq N_M$, the number of harmonics treated by the non-convolution terms of TBC, and construct matrices $\mathbf{P}_1^e$, $\mathbf{P}_0^e$ of a lager dimension: $N_{M_H} \times N_{M_H}$ instead of $N_M \times N_M$ [1]. This is made by extrapolating the entries along the diagonals of the matrixes, see Figure 3, to obtain a band matrix. The extrapolation uses a linear low with respect to the index k of a matrix diagonal $(i+k, j+k)$ where i, j are fixed. It is possible because of correspondent linear asymptotics observed in $\mathbf{P}_1$, $\mathbf{P}_0$. Figure 4 illustrates this behavior on the example of several entries of the matrix $\mathbf{P}_0$. Note that for isotropic case this linear low can be derived analytically.

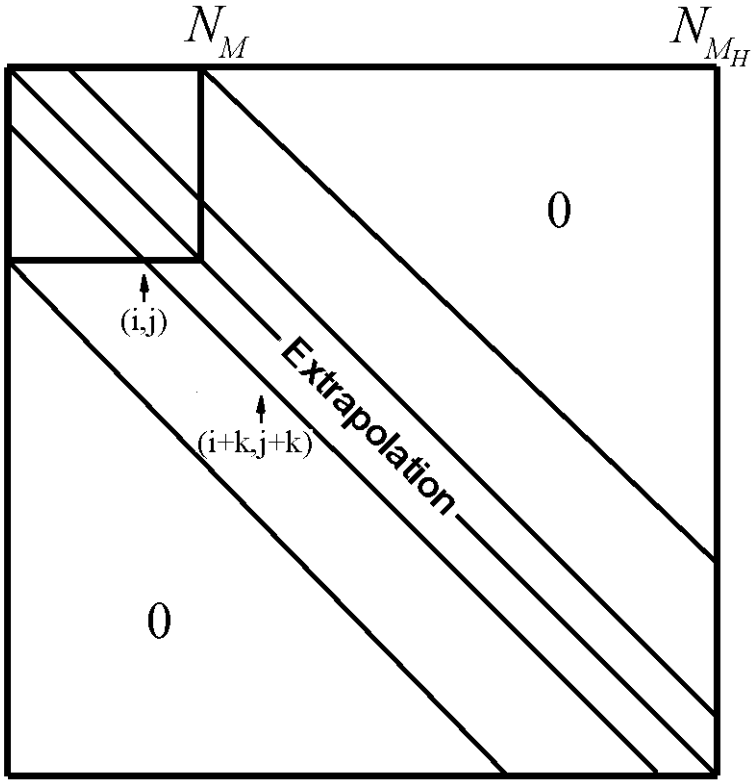

Figure 3. Band $N_{M_H} \times N_{M_H}$ matrices $\mathbf{P}_1^e$, $\mathbf{P}_0^e$ after diagonal extrapolation of original $N_M \times N_M$ matrixes $\mathbf{P}_1$, $\mathbf{P}_0$

The reason of introducing $N_{M_H} \geq N_M$ is motivated by wish of a more accurate treatment of higher harmonics (underline that our TBC operator treats all harmonics with numbers larger than N_{M_H} by just uniform Dirichlet condition).

[1] This is dimension in terms of blocks: actually each entry of the matrices is a 4x4 block; so the exact dimension of the matrices is $(4N_M + 2) \times (4N_M + 2)$

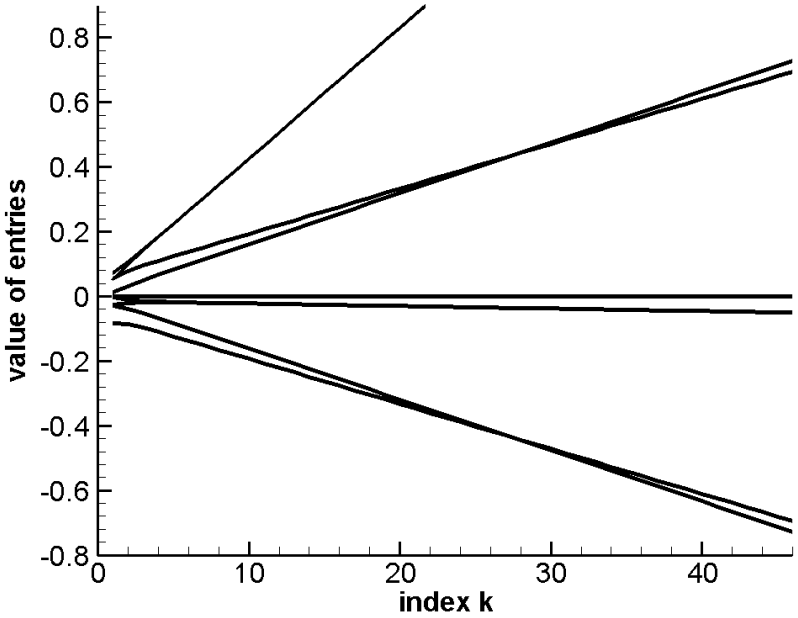

Figure 4. Typical behavior of entries of the matrix $\mathbf{P}_0$ depending on k

We generate additional matrices $\mathbf{Q}_{M_H}^{-1}$, $\mathbf{Q}_{M_H}$ similarly to $\mathbf{Q}_M^{-1}$, $\mathbf{Q}_M$ (13). Using *a)* these matrices of the discrete Fourier transform for vector-functions $f = (v_r, v_\theta)$ on the grid (12), *b)* extrapolated band matrices $\mathbf{P}_1^e$, $\mathbf{P}_0^e$, and *c)* matrix kernels $\tilde{\mathbf{K}}(t)$, we write out our approximate TBC:

$$\mathbf{Q}_{M_H}^{-1}\mathbf{P}_1^e\mathbf{Q}_{M_H}\frac{\partial f}{\partial t} - \frac{\partial f}{\partial n} + \mathbf{Q}_{M_H}^{-1}\mathbf{P}_0^e\mathbf{Q}_{M_H}f + \mathbf{Q}_M^{-1}\left\{\tilde{\mathbf{K}}(t)*\right\}\mathbf{Q}_M f = 0. \qquad (14)$$

§ 3. Solution of elliptic problems obtained after Laplace transform

In order to approximate differential operators $\frac{\partial}{\partial\theta}$, $\frac{\partial^2}{\partial\theta^2}$ on a uniform periodical grid we use the pseudo-spectral approximation.

Let introduce the grid in the azimuth direction

$$\theta_k = k\frac{2\pi}{N_\theta},\ k = 1,\ldots,N_\theta,$$

where N_θ is even. then for functions given in these nodes the following matrices of numerical differentiation are applied:

$$D^{(1)}_{i,j} = \frac{(-1)^{i-j}}{2}\cot\big((i-j)\pi/N_\theta\big), \quad i \neq j$$

for the first derivative, and

$$D^{(2)}_{i,j} = \frac{(-1)^{i-j+1}}{2}\frac{1}{\sin^2\big((i-j)\pi/N_\theta\big)}, \quad i \neq j,$$

$$D^{(2)}_{i,i} = -\frac{N_\theta^2+2}{12}$$

for the second one. It is simply established (from the definition of the matrices, in fact) that the first-order differentiation is exact for the set of conventional Fourier basis functions

$$\{\sin m\theta\}_{m=1}^{N_\theta/2-2}, \ \{\cos m\theta\}_{m=0}^{N_\theta/2-1}$$

i.e. for $N_\theta - 2 = (N_\theta/2 - 2 + N_\theta/2)$ functions. That is why we need two extra grid points to handle correctly discrete periodic functions given by the finite Fourier series

$$f(\theta_k) = \sum_{m=1}^{N_M-1} f_m^{si}\sin(m\theta_k) + \sum_{m=0}^{N_M} f_m^{co}\cos(m\theta_k)$$

i.e. $N_\theta = 2N_M + 2$.

An exponential grid is used in the radial direction, shifted for half spacing from the boundaries:

$$r_i = R_\Gamma + (R_{\max} - R_\Gamma)\frac{e^{\alpha i h} - e^{0.5\alpha h}}{e^{\alpha(1-0.5h)} - e^{0.5\alpha h}}, \quad h = 1/N_r, \quad i = 0,\ldots,N_r \quad (15)$$

Here $R_{\max}$ is the outer boundary of the computational domain of the auxiliary problem shown in Figure 2.

The magnitude of $R_{\max}$ depends strongly on s_j if we put homogeneous Dirichlet conditions at $R_{\max}$ while approximating condition at infinity in (9). Approximately $R_{\max} - R_\Gamma = O(1/s_j)$.

Three-point central finite differences in radial direction are used to approximate governing equations on the grid (15), the parametric differentiation is made wrt $\chi = ih$ mapping $[h/2,\ 1-h/2] \mapsto [R_\Gamma, R_{\max}]$.

The correspondent system of linear equations is then solved by the "matrix progonka" method in radial direction. Evidently, the matrices in $\theta-$direction are dense because of the pseudo-spectral differentiation. Therefore, the computational costs of this direct method are estimated by the value $O(N_r N_\theta^3)$. Although the latter is big enough, the advantage is that "matrix progonka" solves simultaneously $4N_M + 2$ BVPs; each of these BVPs corresponds to a single discrete basis function $\varphi^m(\theta)$ in (13). Besides, the solution of the discrete equations is obtained with the machine accuracy.

After solution of these $4N_M + 2$ BVPs we have $4N_M + 2$ discrete functions $\frac{\partial}{\partial r}\hat{f}^m(r,\theta)$ on Γ in grid points (12). Decomposing them into Fourier components by the operator $\mathbf{Q}_M$, see (13), we obtain the discrete matrix $\hat{P}_n^m(s_j)$, $n, m = 1, \ldots, 4N_M + 2$.

Numerical inverse Laplace transform requires high accurate estimation of $\hat{P}_n^m(s_j)$. That is why we use Richardson extrapolation to increase and control the accuracy. The process is as follows. Fix desired accuracy ε.

a) Fix parameter N_θ (evidently, $N_\theta \geq 4N_M + 2$).

b) Fix initial guess of α and initial guess of $w_j = R_{\max} - R_\Gamma$ in (15).

c) Consider $R_{\max}$ successively for w_j, $2w_j$, $4w_j$, ... ;

d) Consider $N_r = 16,\ 32,\ 64, \ldots$ for given $R_{\max}$, calculate correspondent $\hat{P}_n^m(s_j)$ and make Richardson extrapolation until the difference Δ_{Nr} between two successive extrapolations decreases. Return to level c) and continue until difference Δ_w between best Richardson extrapolations for neighbor $R_{\max}$ decreases. Break if $\Delta_w < \varepsilon$.

Here indents mark nested loops. Evidently, the above process provides the so-called internal mesh convergence (control of Δ_{Nr}), as well as convergence with respect to $R_{\max}$ (control of Δ_w).

Remark 1. The value of α is also varied on the level d) if required.

Remark 2. Values of Δ_{Nr} and Δ_w are estimated by *C*-norm over all entries of $\hat{P}_n^m(s_j)$.

Remark 3. Richardson extrapolation is made under assumption that discrete solution has $O(h^2)$ accuracy:

```
for p=1:pmax
    f_{p,0}=solution_p
    for order=1:p
        f_{p,order}=(2^{order+1}f_{p,order-1}-f_{p-1,order-1})/(2^{order+1}-1)
    end
end
```

Here $\mathrm{solution_p}$ is $\hat{P}_n^m(s_j)$ calculated on the grid with $N_r = 16 * 2^{p-1}$; $\mathrm{f_{p,order}}$ is Richardson extrapolant; pmax is the maximal number of grid refinement.

*Remark*4. Inclusion of the level a) into the internal mesh convergence control by successive increasing N_θ is also possible.

§ 4. Approximation of the *DtN* Matrix

Algorithm briefly described in the previous section allows to compute *DtN* matrix $\hat{P}_n^m$ for any s. In this section we consider each element of the *DtN* matrix as a function $f(s)$ in the dual Laplace space, it is necessary to come back to the physical space, i.e. to calculate its inverse Laplace transform $g(t)$ in time domain. Generally, it is not possible to get exact $g(t)$. Moreover, we only know approximate values of $f(s)$ in several points on the real axis. Our approach consists of approximation of $f(s)$ by a sum of functions that have exact inverse Laplace transform.

Because of the second order of the governing equations the functions in the *DtN* matrix have linear asymptotic, $f(s) \approx p_1 s + p_0$ as $s \to \infty$.

A reasonable choice of approximating the decaying remainder after subtraction of the linear part is rational functions:

$$f(s) \approx \tilde{f}(s) = \mathrm{Re} \sum_{\ell=1}^{L} \frac{\alpha_\ell}{s - \beta_\ell} + p_1 s + p_0 .$$

The corresponding time-domain kernel is

$$\tilde{g}(t) = \operatorname{Re} \sum_{\ell=1}^{L} \alpha_\ell \, \mathrm{e}^{\beta_\ell t} + p_1 \delta'(t) + p_0 \delta(t).$$

We call the coefficients $\beta_\ell \in \mathbb{C}$ the *poles* of the approximations, and coefficients $\alpha_\ell \in \mathbb{C}$ the *weights* of those poles.

Due to physical considerations, the exponentials in $\tilde{g}(t)$ must be decaying, i.e. $\operatorname{Re}\beta_\ell < 0$. We may assume that $\operatorname{Im}\beta_\ell \geq 0$ (because we can replace α_ℓ, β_ℓ with their conjugates and $\hat{g}(t)$ will not change). From the numerical point of view, it is desirable that the decay and the oscillations of the exponentials are not too fast, i.e. $\operatorname{Re}\beta_\ell \geq \beta^r_{\min}$ and $\operatorname{Im}\beta_\ell \leq \beta^i_{\max}$. Generally, the poles of the approximation must meet the following requirements:

$$\beta^r_{\min} \leq \operatorname{Re}\beta_\ell < 0, \; 0 \leq \operatorname{Im}\beta_\ell \leq \beta^i_{\max}.$$

Note that determination of the unknown coefficients p_1 and p_0 is also made by using rational functions approximation technique.

A common tool of the rational approximation is the Chebyshev-Padé algorithm. It can produce approximations of very high accuracy. However, it has significant drawback: the linear system arising in this algorithm is extremely ill-conditioned. Unfortunately, this is a fundamental issue caused by the unboundness of the inverse Laplace transformation in the considered class of functions. The consequence of the latter is the fact that even small perturbations of the functions being approximated can lead to the appearance of poles with $\operatorname{Re}\beta_\ell > 0$. Sometimes such poles may be avoided by changing the value of L, but it cannot be guaranteed.

The coefficients p_1, p_0 are determined before looking for the poles as we shall show further.

Algorithm Overview

The main part of the approximation algorithm is as follows:

1) Change of variables ("*inversion*") from s to σ which translated the ray $[0,\infty)$ in s to line segment $(0,1]$ in σ. This change of variable is characterized by parameter a (the *center of inversion*).
2) Calculate $f(\sigma)$ in Chebyshev's nodes on $(0,1)$.
3) Calculate Chebyshev's coefficients of f.
4) Estimate linear asymptotic $p_1\sigma + p_0$.
5) Extract linear asymptotic from $f(\sigma) = f_1(\sigma) + p_1\sigma + p_0$.
6) Apply Chebyshev-Padé algorithm:

$$f_1(\sigma) \approx \tilde{f}_1(\sigma) = \frac{P(\sigma)}{Q(\sigma)}.$$

7) Do a partial fraction expansion:

$$\tilde{f}_1(\sigma) = \mathrm{Re}\sum_{\ell=1}^{L}\frac{\alpha_{\sigma,\ell}}{\sigma-\beta_{\sigma,\ell}}.$$

8) Return to variable s:

$$f(s) \approx p_1 s + p_0 + \mathrm{Re}\sum_{\ell=1}^{L}\frac{\alpha_\ell}{s-\beta_\ell}.$$

9) If there are poles with $\mathrm{Re}\,\beta_\ell < \beta_{\min}^r$
   a) correct p_0 , i.e. for each such pole set

$$p_0 := p_0 - \mathrm{Re}\frac{\alpha_\ell}{\beta_\ell}.$$

   b) go to step 5 (unless the number of iterations is exceeded).
10) If there are poles outside of the desired box, reject them.
11) Do a least-squares fit for weights α_ℓ.
12) Fit random poles:
   a) Select a new pole in the desired box for β.
   b) Do a least-squares fit for weights α_ℓ.
   c) If the residual has decreased by a factor of at least $0{,}9$, add this new pole to the old ones.
   d) Go to step a.

Inversion

The formula for inversion is

$$s = a\frac{1-\sigma}{\sigma}, \quad \sigma = \frac{a}{s+a}.$$

Rational approximation in σ and s

$$f(s) = p_1 s + p_0 + \mathrm{Re}\sum_{\ell=1}^{L}\frac{\alpha_\ell}{s-\beta_\ell}, \quad f(\sigma) = \mathrm{Re}\sum_{\ell=1}^{L}\frac{\alpha_{\sigma,\ell}}{\sigma-\beta_{\sigma,\ell}}$$

are related by

$$\alpha_\ell = -\frac{a\alpha_{\sigma,\ell}}{\beta_{\sigma,\ell}^2}, \quad \beta_\ell = a\frac{1-\beta_{\sigma,\ell}}{\beta_{\sigma,\ell}}, \quad p_0 = -\sum_{\ell=1}^{L} \mathrm{Re}\,\frac{\alpha_{\sigma,\ell}}{\beta_{\sigma,\ell}}.$$

Ratios of polynomials in σ and s

$$f(s) = \frac{P(s)}{Q(s)}, \quad f(\sigma) = \frac{\Pi(\sigma)}{\Theta(\sigma)}$$

are related by

$$P(s) = \sum_{k=0}^{\deg\Pi} \Pi_k a^k (s+a)^{N-k}, \quad Q(s) = \sum_{k=0}^{\deg\Theta} \Theta_k a^k (s+a)^{N-k}.$$

Calculation of Chebyshev's Nodes and Coefficients

Calculation of Chebyshev's Nodes and Coefficients consists of the following steps.

1. Fix a natural number N, usually $N \geq 8L$, where L is the desired number of poles.
2. Chebyshev's nodes in σ are

$$\sigma_n = \frac{1}{2}\left(1 - \cos\pi\frac{n+\frac{1}{2}}{N+1}\right), \quad n = 0,\ldots,N.$$

3. Calculate corresponding values of s, the set s_n.
4. Calculate $f_n = f(s_n)$, $n = 0,\ldots,N$.
5. Calculate $N+1$ Chebyshev's coefficients of f:

$$f_n^C = \frac{1+\delta_{n,0}}{N+1}\sum_{j=0}^{N} f_n \cos\pi\frac{j\left(n+\frac{1}{2}\right)}{N+1}.$$

This is a linear operation, which means it may be interpreted as multiplication of vector $(f_0,\ldots,f_N)$ by a matrix with appropriate entries.

Estimation of Linear Asymptotic with respect to s

For given K and ΔK calculation of the linear part of $f(s)$ consists of the following steps.

First, we apply Chebyshev-Padé algorithm and obtain

$$f(\sigma) = \frac{P(\sigma)}{Q(\sigma)}, \quad \deg P = K + \Delta K, \quad \deg Q = K.$$

Then coefficients of linear parts of $f(s)$

$$p_1 = \frac{r_0}{a}, \quad p_0 = r_0 + r_1,$$

where

$$r_0 = \left.\frac{P(\sigma)}{Q(\sigma)}\right|_{\sigma=0}, \quad r_1 = \left.\left(\frac{P(\sigma)}{Q(\sigma)}\right)'\right|_{\sigma=0}.$$

But the best choice of K is not known a priori. Algorithm for adjusting K is the following.

1. Set $p_{1,K_{\min}-1} = 0,\ p_{0,K_{\min}-1} = 0$.
2. Repeat for K from $K_{\min}$ to $K_{\max}$:
   a. Find $p_{1,K},\ p_{0,K}$ by the main algorithm.
   b. Calculate $\delta_K = \left(p_{1,K-1} - p_{1,K}\right)^2 + \left(p_{0,K-1} - p_{0,K}\right)^2$.
3. Choose K^* where δ_K is minimal.
4. Set $p_1 = p_{1,K^*},\ p_0 = p_{0,K^*}$.

Partial Fraction Expansion

To represent a ratio of polynomials $f(s) = P(s)/Q(s)$ as a sum of rational functions, we do the following:

1. Find roots β_ℓ of $Q(s)$.
2. Discard all roots with $\operatorname{Im}\beta_\ell < 0$.
3. For each pole β_ℓ set

$$\alpha_\ell = c\frac{P(\beta_\ell)}{Q'(\beta_\ell)}$$

where $c = 1$ if $\operatorname{Im}\beta_\ell = 0$ and $c = 2$ otherwise. This is true since $\alpha_\ell = \left.\left((s-\beta_\ell) f(s)\right)\right|_{s=\beta_\ell}$, $Q(s) = (s-\beta_\ell)Q_1(s)$, $Q'(\beta_\ell) = Q_1(\beta_\ell)$.

Linear Fitting of α, p

It is easily seen that $\hat{f}(s;\alpha,\beta,p)$ is linear function of α, p. Therefore, the problem

$$r^2\left(\alpha,\hat{\beta},p\right)=\tfrac{1}{2}\left\|f(\cdot)-\hat{f}\left(\cdot;\alpha,\hat{\beta},p\right)\right\|^2\to\min_{\alpha,p}$$

for a fixed $\hat{\beta}$ is a linear least squares problem. Unfortunately, it leads to an ill-conditioned system of linear equations. To overcome this, we apply regularization and solve the following problem:

$$\tfrac{1}{2}\left\|f(\cdot)-\hat{f}\left(\cdot;\alpha,\hat{\beta},p\right)\right\|^2+\tfrac{1}{2}\varepsilon\left(\left\|\alpha-\hat{\alpha}\right\|^2+\left\|p-\hat{p}\right\|^2\right)\to\min_{\alpha,p}$$

where $\hat{\alpha}$, $\hat{\beta}$, and $\hat{p}$ are the values obtained using the optimization described in previous section. $\varepsilon>0$ is a regularization parameter that should be smaller than the desired level of accuracy.

The described technique reduces rapidly the residual r^2 by several orders of magnitude sometimes.

Again, there is an option of fitting only α with fixed $p=\hat{p}$.

§ 5. Time-domain solver in the annulus

We describe here setup and several discretization aspects of the test problems used for verifying our TBC.

Governing equations are implemented in the polar system of coordinates. In order to avoid issues with discretization and calculations at the origin we consider the task in an annulus. The setup is as shown in Figure 5, where

- radius R_0 corresponds to the internal boundary where we prescribe Dirichlet boundary conditions to initiate elastic waves (initial data of solution in the annulus are zero);
- Γ with radius R_Γ is the external boundary where we put our transparent boundary conditions.

The verification of TBC is made by comparing solution of this problem with the solution of a second problem having a much bigger external radius R_{ext} (extended domain), so the reflections from this boundary achieve Γ after a definite (long) time of simulation.

We use the polar spatial grid

$$r_i=R_0+ih_r,\quad h_r=\frac{R_\Gamma-R_0}{N_R},\quad i=0,1,\ldots,N_R$$

$$\theta_j = jh_\theta, \quad h_\theta = \frac{2\pi}{N_\theta}, \quad j = 0,1,,\ldots, N_\theta - 1$$

and the temporal grid

$$t^k = k\tau, \quad k = 0,1,\ldots$$

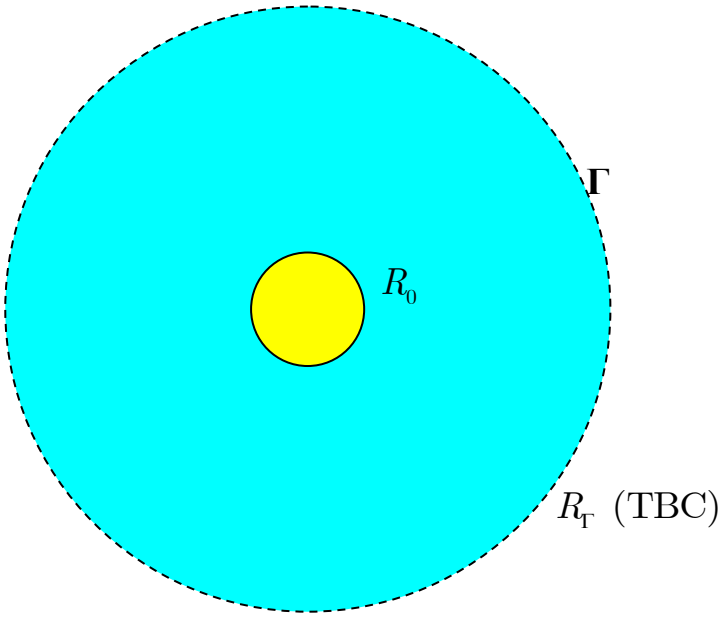

Figure 5. Setup of the test problem in the annulus

Equation (7) is approximated by the usual explicit second-order central-difference scheme with unknown functions defined in the nodes (t^k, r_i, θ_j). Below we describe implementation of the TBC operator in frames of explicit difference schemes integrating the elastodynamics equations.

Ideology of explicit scheme yields the following approach of incorporation of the TBC operator into the algorithm: having the solution at the time levels $\ldots, t^{k-2}$, t^{k-1}, t^k, we firstly update the solution in the internal points by using the difference scheme; then we update the solution at the boundary Γ using the TBC operator.

Let us consider this second step. Operator of TBC reads

$$\mathbf{Q}_M^{-1}\mathbf{P}_1\mathbf{Q}_M \frac{\partial f}{\partial t} - \frac{\partial f}{\partial n} + \mathbf{Q}_M^{-1}\mathbf{P}_0\mathbf{Q}_M f + \mathbf{Q}_M^{-1}\left\{\tilde{\mathbf{K}}(t) * \right\}\mathbf{Q}_M f = 0 \qquad (16)$$

where $\mathbf{Q}_M^{-1}$, $\mathbf{Q}_M$ are matrices of the discrete Fourier transform for the vector-functions $f = (v_r, v_\theta)$ in sin-cos basis; $\mathbf{P}_1$, $\mathbf{P}_0$ are given constant matrices in Fourier space, and the matrix $\tilde{\mathbf{K}}(t)$ with entries

$$\tilde{K}_n^m(t) \equiv \sum_{l=1}^{L_n^m} \alpha_{n\,l}^m \exp(\beta_{n\,l}^m t), \qquad \mathrm{Re}(\beta_{n\,l}^m) \le \delta < 0 \tag{17}$$

contains given kernels of convolutions.

After the first step (update in internal grid points) we know solution in points drawn in Figure 6 by circles, (θ – direction, normal to the figure plane, is not shown).

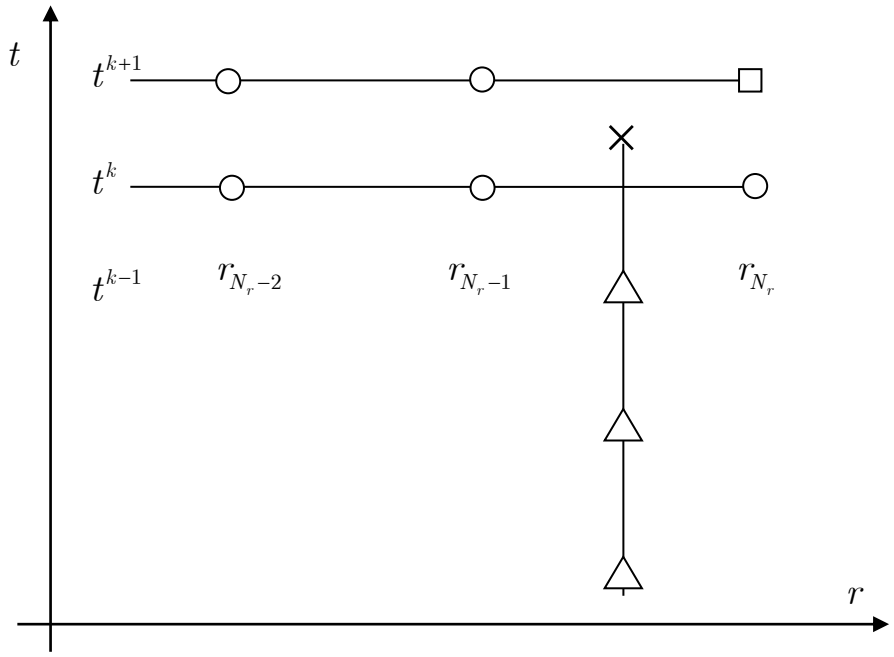

Figure 6. Grid setup for approximation of TBC

The aim is to update the solution f_{Nr}^{k+1} at the square point by using (16). First we calculate the Fourier coefficients $\hat{f} \equiv \{f^m\}_{m=0}^M$ of f in points with $r = r_{N_r-1}$ and $r = r_{N_r}$ by using matrix $\mathbf{Q}_M$. Then we consider the central-difference discretization of TBC

$$\mathbf{P}_1 \frac{\partial \hat{f}}{\partial t} - \frac{\partial \hat{f}}{\partial r} + \mathbf{P}_0 \hat{f} + \left\{\tilde{\mathbf{K}}(t) * \right\} \hat{f} = 0 \tag{18}$$

in the Fourier space for the central point (cross in the figure). First three terms in (18) are approximated by

$$\frac{\partial \hat{f}}{\partial t} \approx \frac{\hat{f}_{Nr}^{k+1} - \hat{f}_{Nr}^{k} + \hat{f}_{Nr-1}^{k+1} - \hat{f}_{Nr-1}^{k}}{2\tau},$$

$$\frac{\partial \hat{f}}{\partial r} \approx \frac{\hat{f}_{Nr}^{k+1} - \hat{f}_{Nr-1}^{k+1} + \hat{f}_{Nr}^{k} - \hat{f}_{Nr-1}^{k}}{2h_r},$$

$$\hat{f} \approx 0.25(\hat{f}_{Nr}^{k+1} + \hat{f}_{Nr-1}^{k+1} + \hat{f}_{Nr}^{k} + \hat{f}_{Nr-1}^{k})$$

with unknown values $\hat{f}_{Nr}^{k+1}$. Provided that the fourth, integral, term is known, we, evidently, can write out a matrix resolution equation for $\hat{f}_{Nr}^{k+1}$ from (18).

Explicit calculation of the integral term in the central point (cross) is made as follows. We consider integration over the interval shown by the vertical line in Figure 6. Using (17) we have for $a(t) \equiv f^m(t)$:

$$\begin{aligned}\tilde{K}_n^m(t+\tau/2) * a(t+\tau/2) &= \sum_{l=1}^{L_n^m} \alpha_{n\,l}^{m} \exp(\beta_{n\,l}^{m}(t+\tau/2)) * a(t+\tau/2) \\ &\equiv \sum_{l=1}^{L_n^m} \alpha_{n\,l}^{m} I_{n\,l}^{m}(t+\tau/2),\end{aligned}$$

where

$$\begin{aligned}I_{n\,l}^{m}(t+\tau/2) &= \exp(\beta_{n\,l}^{m}\tau) I_{n\,l}^{m}(t-\tau/2) \\ &\quad + \int_{t-\tau/2}^{t+\tau/2} \exp(\beta_{n\,l}^{m}(t+\tau/2-t')) a(t')dt'.\end{aligned} \tag{19}$$

The integral in (19) is approximated by the Simpson rule:

$$\begin{aligned}\int_{t-\tau/2}^{t+\tau/2} \exp(\beta_{n\,l}^{m}(t+\tau/2-t')) a(t')dt' &\approx \frac{\tau}{6}\exp(\beta_{n\,l}^{m}\tau) a_{-0.5} \\ &\quad + \frac{2\tau}{3}\exp(0.5\beta_{n\,l}^{m}\tau) a_0 \\ &\quad + \frac{\tau}{6} a_{0.5},\end{aligned}$$

where

$$a_{-0.5} \equiv 0.5([f^m]^k_{Nr-1} + [f^m]^{k-1}_{Nr})$$
$$a_0 \equiv 0.5([f^m]^k_{Nr-1} + [f^m]^k_{Nr})$$
$$a_{0.5} \equiv 0.5([f^m]^{k+1}_{Nr-1} + [f^m]^k_{Nr})$$

Thus the Fourier coefficients $\hat{f}^{k+1}_{Nr}$ are known. After this we calculate $f^{k+1}_{Nr} = \mathbf{Q}^{-1}_M \hat{f}^{k+1}_{Nr}$.

Notice that (19) provides recurrent calculations of elementary convolutions $I^m_{n\,l}(t + \tau/2)$.

§ 6. Numerical examples

We put the density $\rho = 1$. List of anisotropic media cases studied in [1], [2] is as follows:

Anisotropic medium I.

$$c^{11} = 4,\ c^{12} = 3.8,\ c^{13} = 0,\ \ c^{22} = 20,\ c^{23} = 0,\ c^{33} = 2$$

Anisotropic medium II.

$$c^{11} = 20,\ c^{12} = 3.8,\ c^{13} = 0,\ \ c^{22} = 20,\ c^{23} = 0,\ c^{33} = 2$$

Anisotropic medium III.

$$c^{11} = 4,\ c^{12} = 4.9,\ c^{13} = 0,\ \ c^{22} = 20,\ c^{23} = 0,\ c^{33} = 2$$

Anisotropic medium IV.

$$c^{11} = 4,\ c^{12} = 7.5,\ c^{13} = 0,\ \ c^{22} = 20,\ c^{23} = 0,\ c^{33} = 2$$

Coefficients c^{ij} are the coefficients in Hooke's law (2).

Note that the case IV cannot be treated by PML at all as shown in [1].

Parameters of the annulus: $R_0 = 2,\ R_\Gamma = 10$. Dirichlet data at R_0 exiting the elastic waves is sum of the first three azimuth harmonics multiplied by a time pulse with the support on the interval $t \in [0,2]$. At $r = R_\Gamma$ we put our TBCs.

We use four grids for test calculations:

- Grid1 (N_θ=100), $h_\theta = \frac{2\pi}{100}$, $h_r = \frac{R_\Gamma - R_0}{50}$
- Grid2 (N_θ=300), $h_\theta = \frac{2\pi}{300}$, $h_r = \frac{R_\Gamma - R_0}{150}$
- Grid3 (N_θ=900), $h_\theta = \frac{2\pi}{900}$, $h_r = \frac{R_\Gamma - R_0}{450}$
- Grid4 (N_θ=2700), $h_\theta = \frac{2\pi}{2700}$, $h_r = \frac{R_\Gamma - R_0}{1350}$

All numerical experiments show low reflection of outgoing waves and the long time stability.

Denote U_{TBC} solutions computed in the computational domain $R_0 \le r \le R_\Gamma \equiv R_{TBC}$, $0 \le \theta \le 2\pi$ with TBCs on boundary $r = R_\Gamma$. For comparison we compute also U_{ext} in the extended domain $R_0 \le r \le R_{ext} = 8R_\Gamma$. Computational grids for the extended domain have the same h_r as grids for domain $R_0 \le r \le R_\Gamma$ with the same N_θ. Figures 7 – 13 show U_{TBC} and restriction of U_{ext} on the domain $R_0 \le r \le R_\Gamma$ for different t for the most difficult medium IV (remind that $U = (v_r, v_\theta)$). One can see that reflections are not visible.

In order to show stability we run calculations until $T = 100$ on Grid2, see Figure 14 and Figure 15. For comparison we compute U_{ref} which is U_{ext} computed on the Grid3 for medium I and is U_{ext} computed on the Grid4 for medium IV. The difference $U_{TBC} - U_{ref}$ until $T = 25$ continued by U_{TBC} at $t > 25$ (where $|| U_{ref} || \ll || U_{TBC} ||$) is shown. We use norms

$$\| U \|_C = \max_\Omega | U |$$

and

$$\| U \|_{L_1} = \frac{1}{N} \sum_\Omega | U |$$

All the cases are stable. However more analysis is necessary.

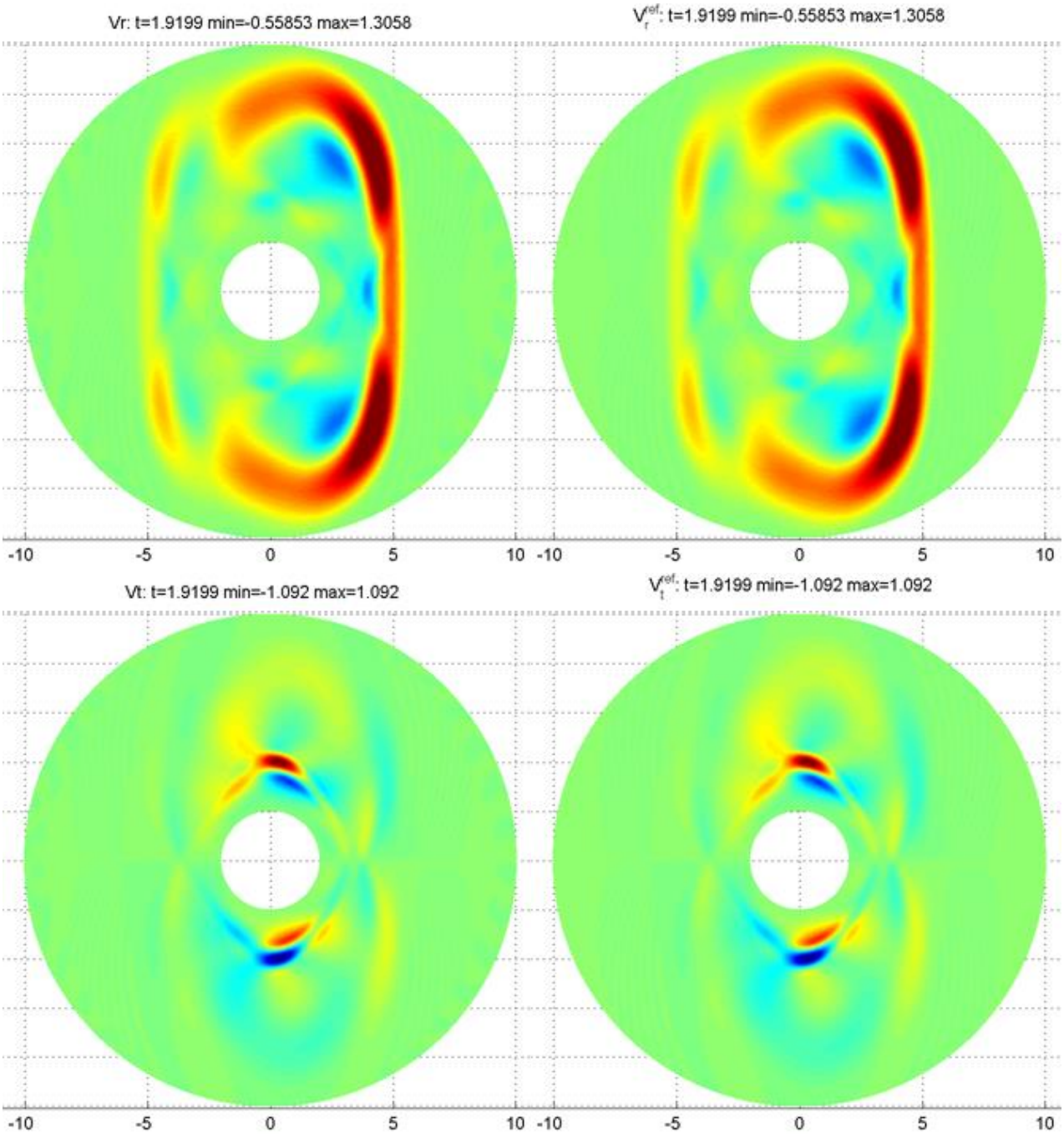

Figure 7. Anisotropic medium IV, t=1.9199: upper left — field of v_r component of U_{TBC}, upper right — field of v_r component of U_{EXT}, lower left — field of v_θ component of U_{TBC}, lower right — field of v_θ component of U_{TBC}

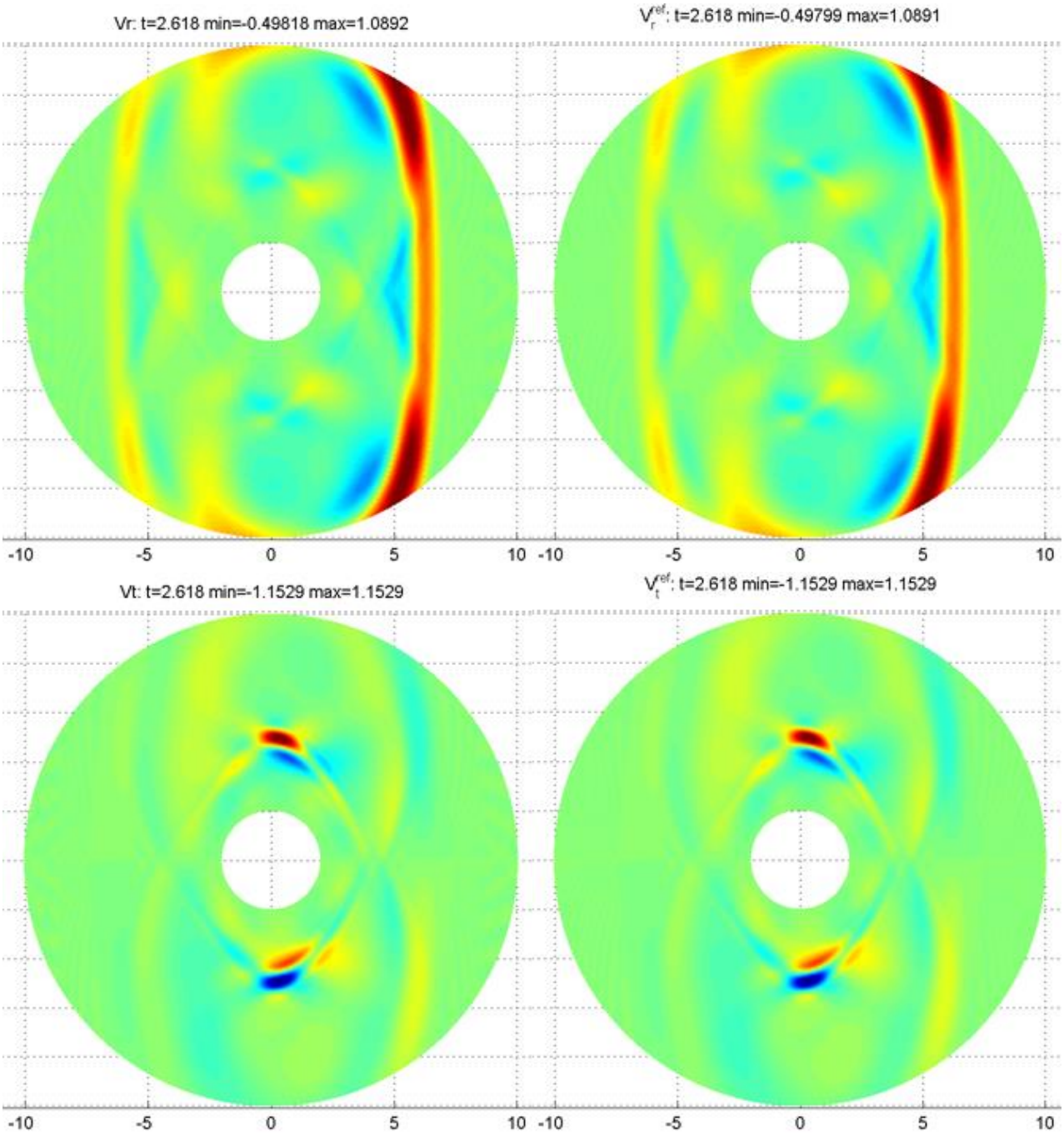

Figure 8. Anisotropic medium IV, t=2.618: upper left — field of v_r component of U_{TBC}, upper right — field of v_r component of U_{EXT}, lower left — field of v_θ component of U_{TBC}, lower right — field of v_θ component of U_{TBC}

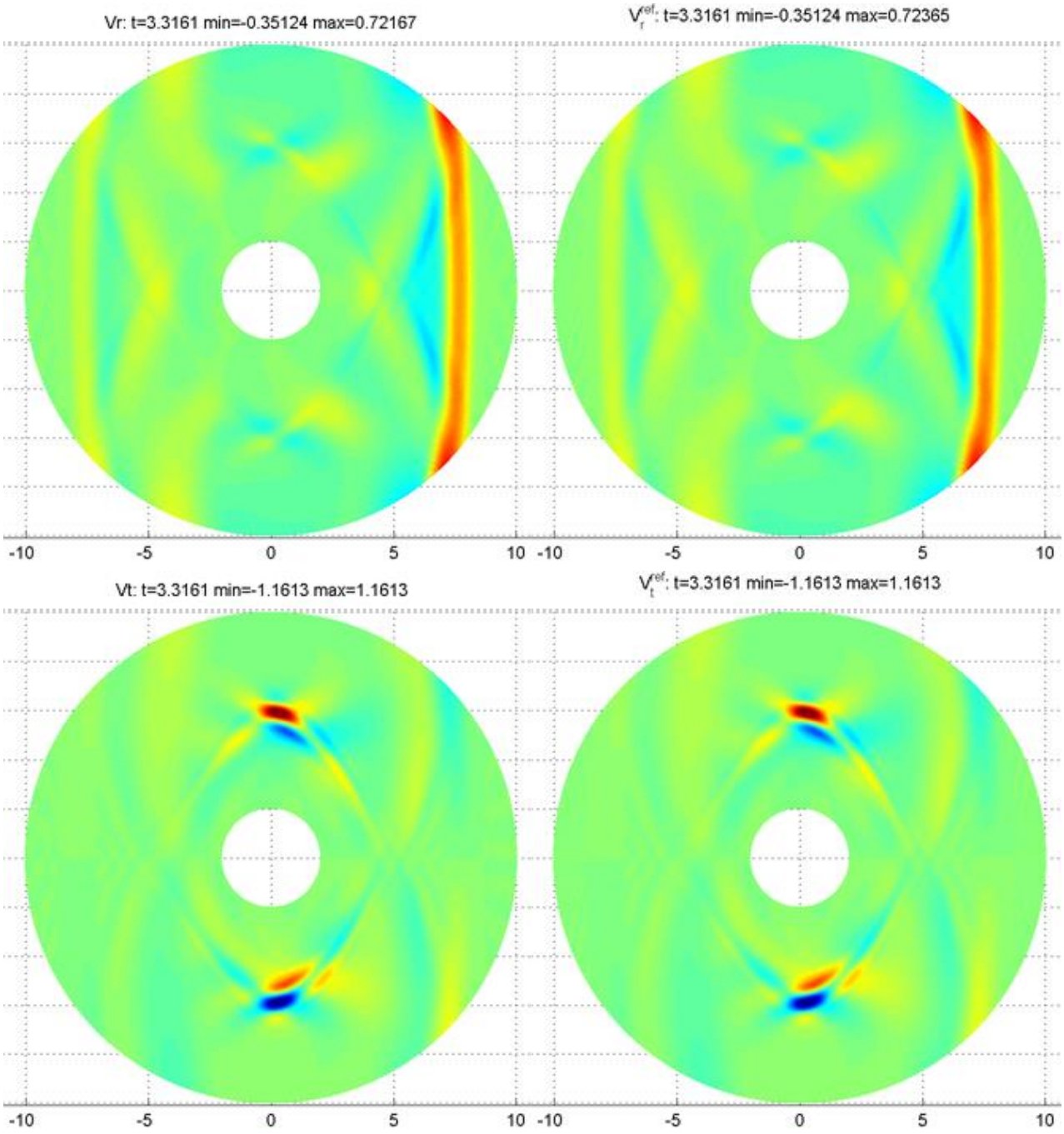

Figure 9. Anisotropic medium IV, t=3.3161: upper left — field of v_r component of U_{TBC}, upper right — field of v_r component of U_{EXT}, lower left — field of v_θ component of U_{TBC}, lower right — field of v_θ component of U_{TBC}

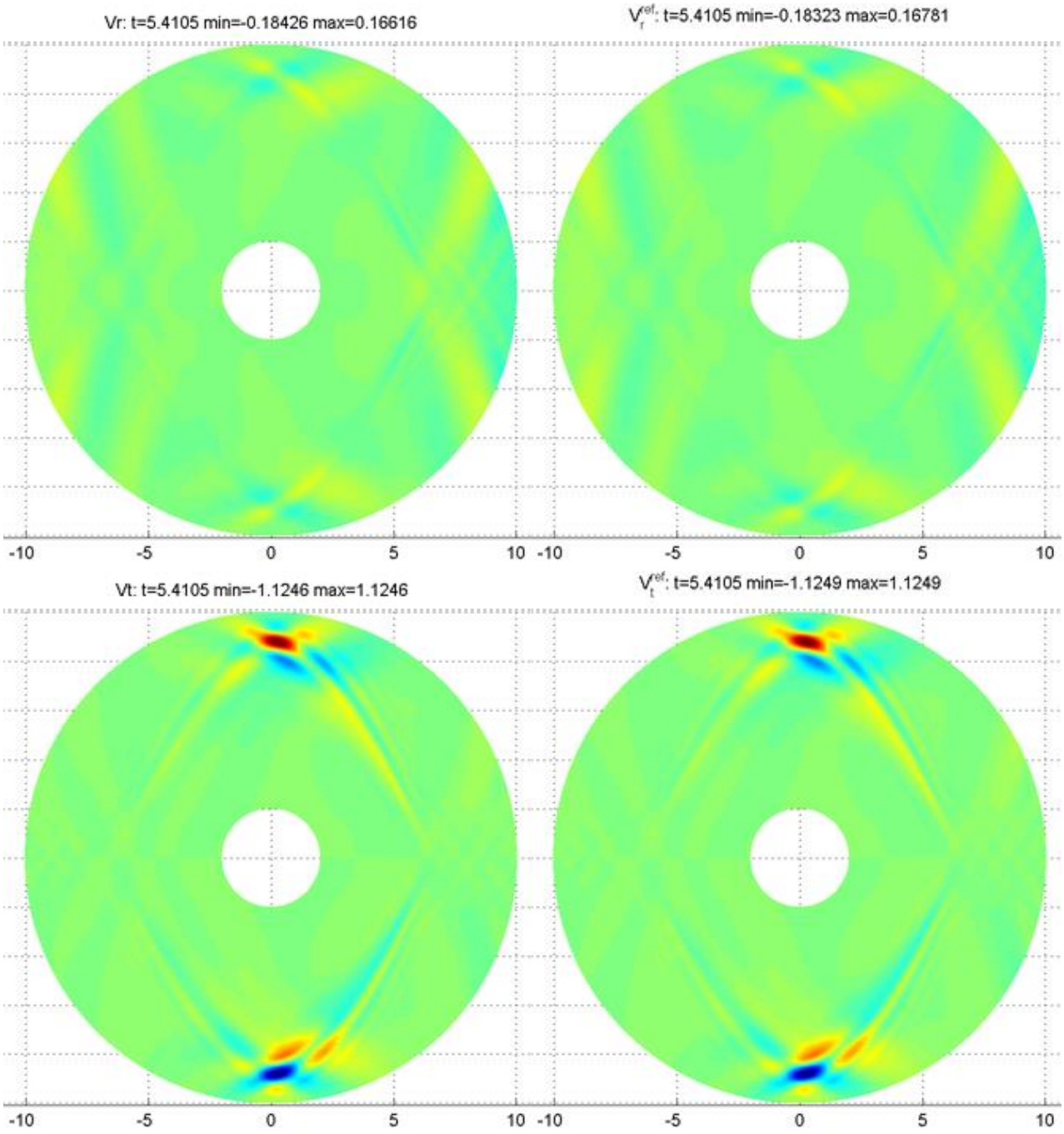

Figure 10. Anisotropic medium IV, t=5.4105: upper left — field of v_r component of U_{TBC}, upper right — field of v_r component of U_{EXT}, lower left — field of v_θ component of U_{TBC}, lower right — field of v_θ component of U_{TBC}

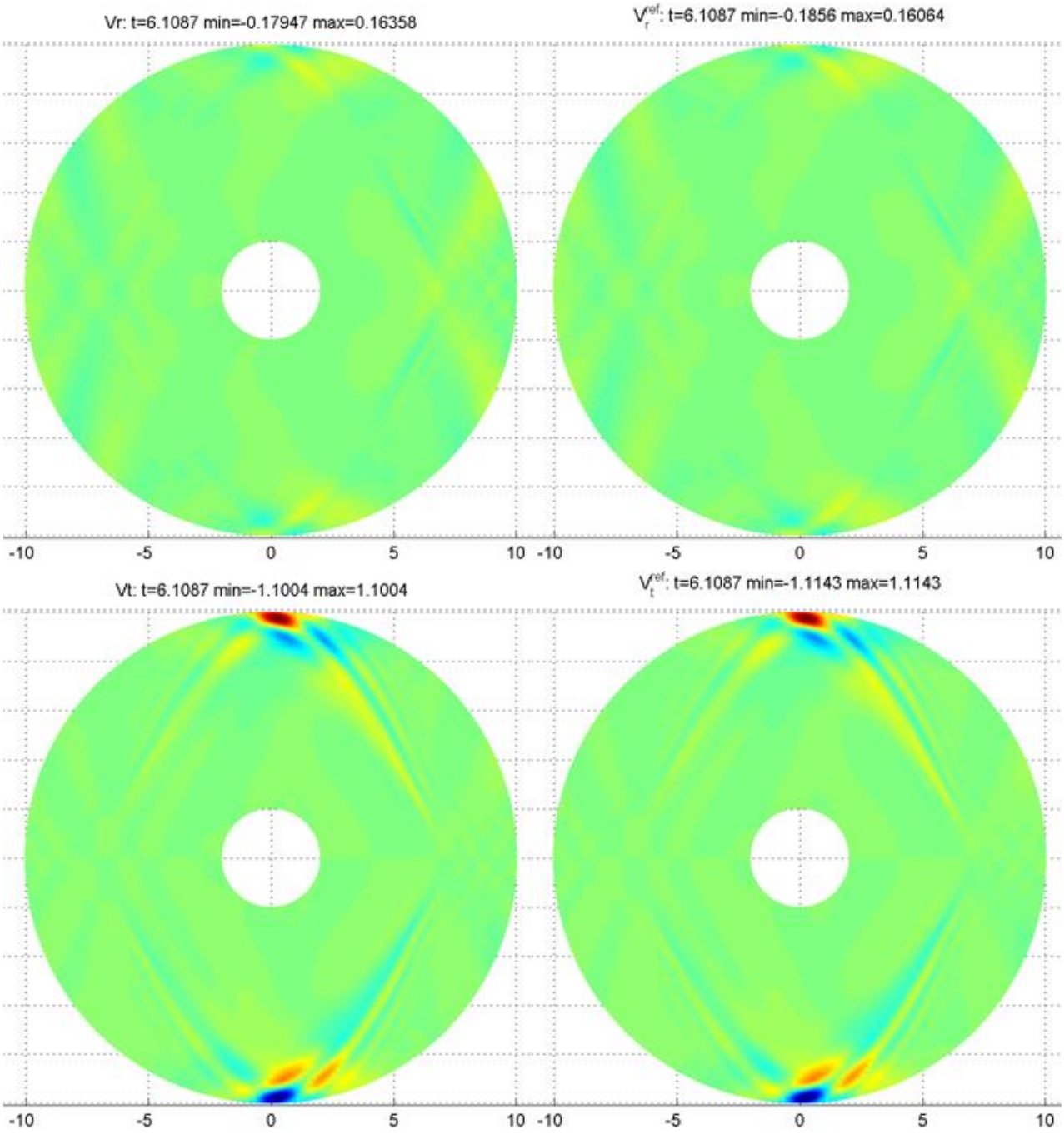

Figure 11. Anisotropic medium IV, t=6.1087: upper left — field of v_r component of U_{TBC}, upper right — field of v_r component of U_{EXT}, lower left — field of v_θ component of U_{TBC}, lower right — field of v_θ component of U_{TBC}

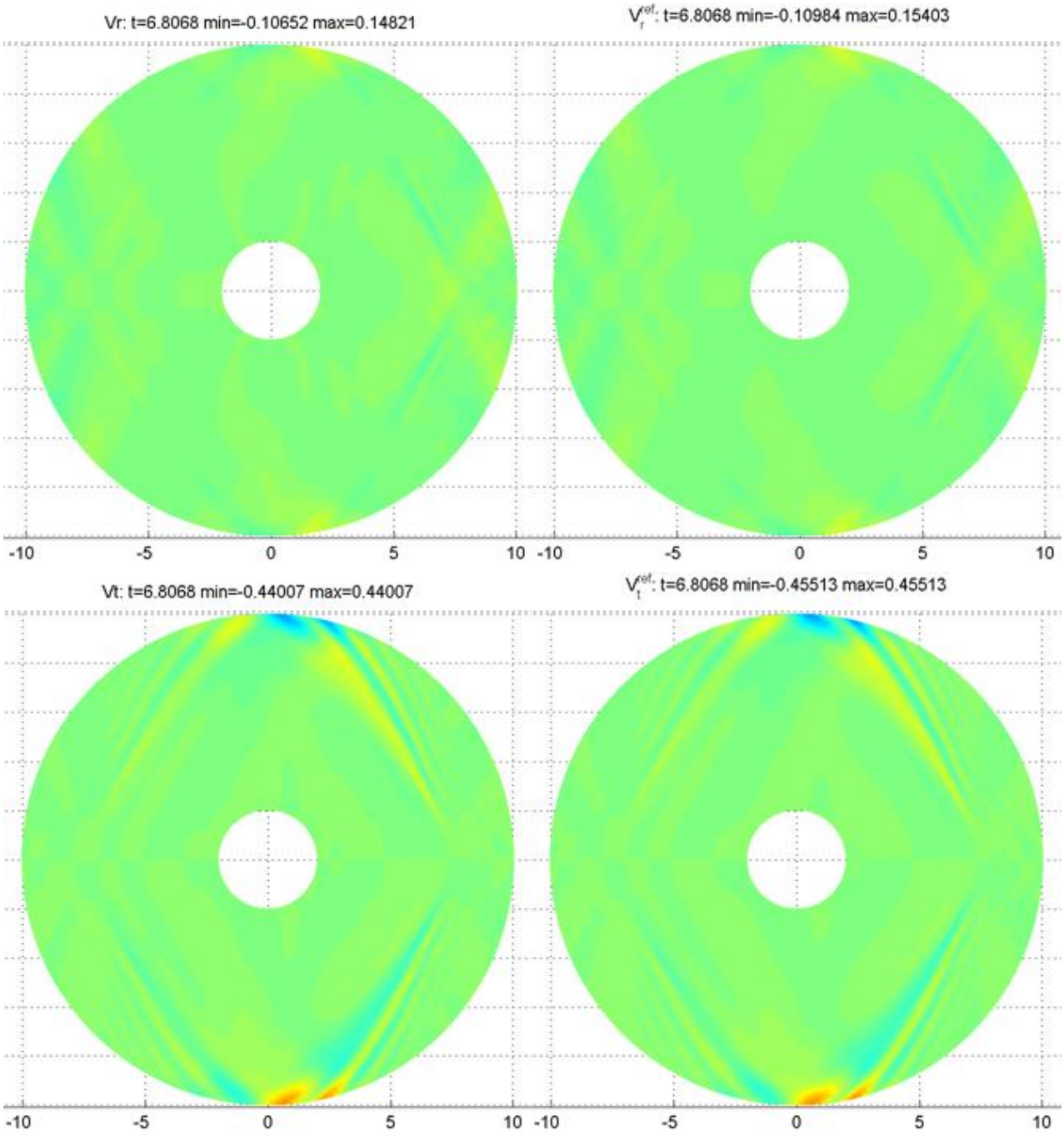

Figure 12. Anisotropic medium IV, t=6.8068: upper left — field of v_r component of U_{TBC}, upper right — field of v_r component of U_{EXT}, lower left — field of v_θ component of U_{TBC}, lower right — field of v_θ component of U_{TBC}

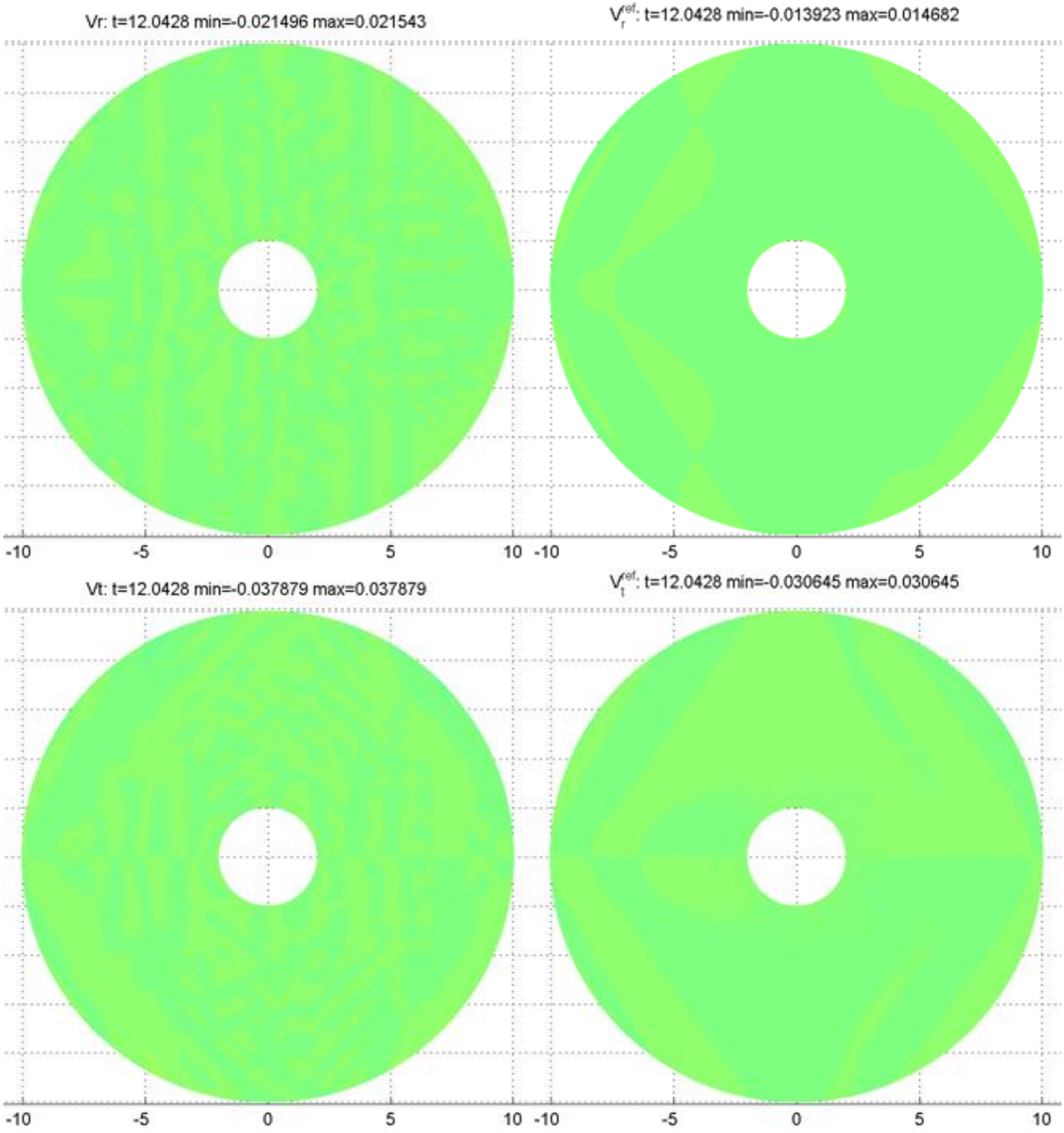

Figure 13. Anisotropic medium IV, t=12.0428: upper left — field of v_r component of U_{TBC}, upper right — field of v_r component of U_{EXT}, lower left — field of v_θ component of U_{TBC}, lower right — field of v_θ component of U_{TBC}

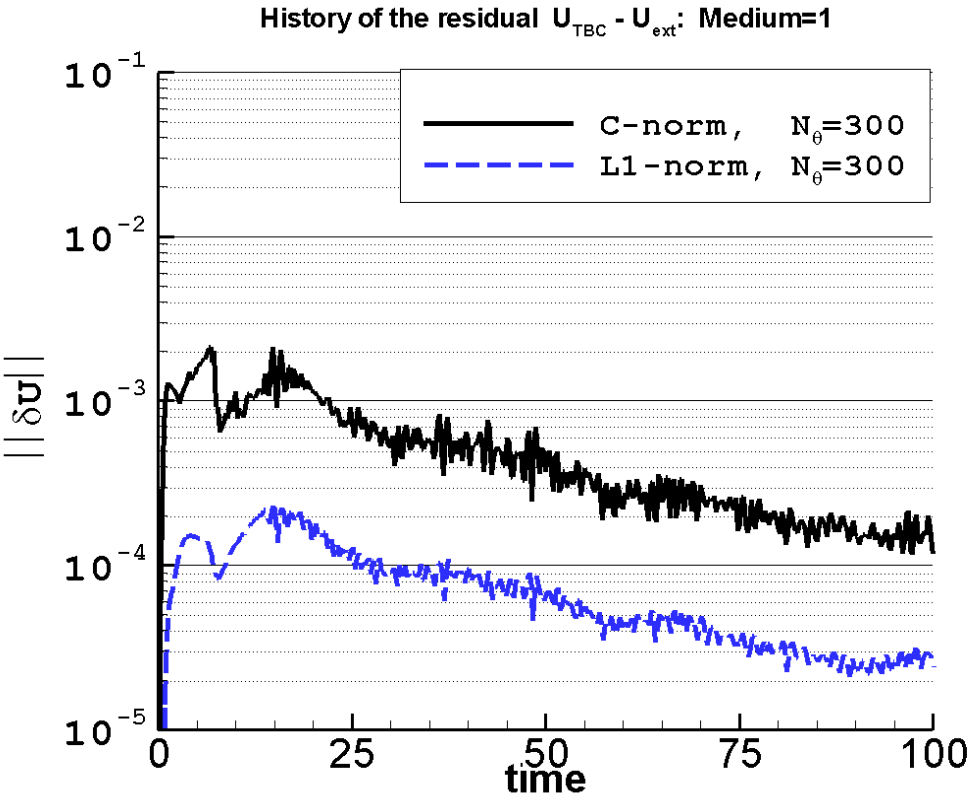

Figure 14. Long-time stability for medium I

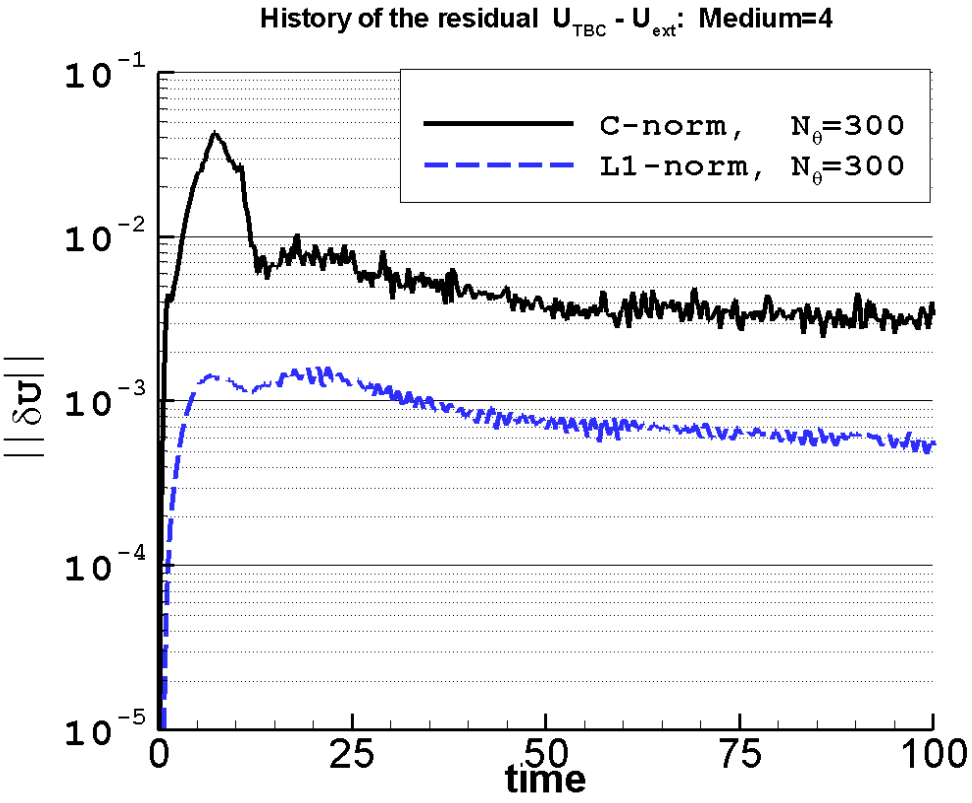

Figure 15. Long-time stability for medium IV

References

[1] Becache E., Fauqueux S., Joly P., Stability of perfectly matched layers group velocities and anisotropic waves, JCP, 188, 2003, 399 – 433;

[2] D. Appelö and G. Kreiss, A New Absorbing Layer for Elastic Waves, Journal of Computational Physics, JCP, 215(2), 2006, 642 – 660.

[3] Sofronov I.L., Zaitsev N.A. Non-reflecting boundary conditions for 2D anisotropic elastodynamics. In: PAMM, Special Issue: GAMM Annual Meeting 2006 – Berlin, 6, Iss. 1, 611–612 (2007), https://doi.org/10.1002/pamm.200610286

[4] Н. А. Зайцев, И. Л. Софронов. Применение прозрачных граничных условий для решения двумерных задач упругости с азимутальной анизотропией // Матем. моделирование, 19:8 (2007), 49–54.